Research Article | Vol. 26, No. 17 | 20 Aug 2018 | OPTICS EXPRESS 21872
Optics EXPRESS

Multipulse instabilities of a femtosecond SESAM-modelocked VECSEL

DOMINIK WALDBURGER,[1,*] CESARE G. E. ALFIERI,[1] SANDRO M. LINK,[1] STEFAN MEINECKE,[2] LINA C. JAURIGUE,[2] KATHY LÜDGE,[2] AND URSULA KELLER[1]

[1]*Department of Physics, Institute for Quantum Electronics, ETH Zürich, 8093 Zürich, Switzerland*
[2]*Institut für Theoretische Physik, TU Berlin, 10623 Berlin, Germany*
[*]*dominikw@phys.ethz.ch*

Abstract: Optically pumped passively modelocked vertical external-cavity surface-emitting lasers (VECSELs) can generate pulses as short as 100 fs with an intracavity semiconductor saturable absorber mirror (SESAM). Very stable soliton modelocking can be obtained, however, the high-Q-cavity, the short gain lifetime, and the kinetic-hole burning can also support rather complex multipulse instabilities which we analyze in more details here. This onset of multipulse operation limits the maximum average output power with fundamental modelocking and occurs at the roll-over of the cavity round trip reflectivity. Unfortunately, such multipulse operation sometimes can mimic stable modelocking when only limited diagnostics are available.

1. Introduction

Optically pumped semiconductor disk lasers (SDLs) are high-power laser sources which convert low-coherence light from pump diode arrays into high brightness beams with excellent quality. Semiconductor bandgap engineering can set the center wavelength of this source from the visible to the mid-infrared [1]. In particular, optically pumped vertical external-cavity surface-emitting lasers (VECSELs) [2] have demonstrated continuous wave (cw) operation with an average output power as high as 20 W in fundamental transverse mode and 106 W in multimode [3,4]. The first ultrafast VECSEL was modelocked with a semiconductor saturable absorber mirror (SESAM) [5] in 2000 [6]. Since then, the performance of ultrafast SDLs has been improved, as summarized in recent reviews [1,7–9]. In SESAM-modelocked operation, pulse repetition rates range from 85 MHz up to 100 GHz [10,11] and emission wavelengths from 489 nm up to 1960 nm have been demonstrated [12,13]. The best performance in terms of power and pulse duration has been achieved in

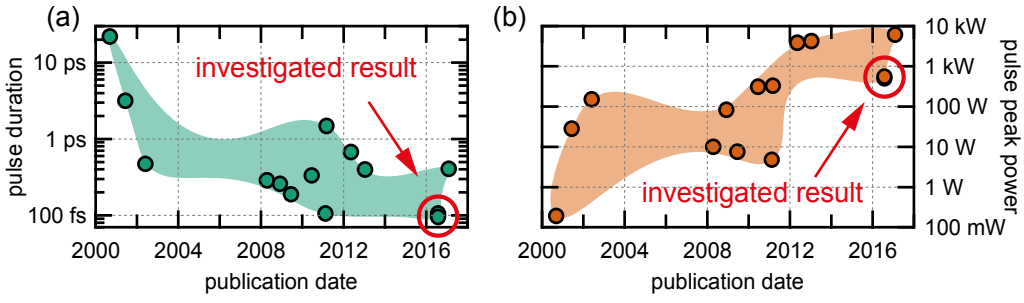

Fig. 1. Timeline of record performance results from SESAM-modelocked optically pumped VECSELs at a center wavelength of around 1 µm in terms of (a) pulse duration and (b) pulse peak power (see references in [1,7–9]). (Red circle) High-power 100-fs modelocking result as described in more details by Waldburger *et al.* [14].

#334220 https://doi.org/10.1364/OE.26.021872
Journal © 2018 Received 5 Jun 2018; revised 27 Jul 2018; accepted 3 Aug 2018; published 8 Aug 2018

Optics EXPRESS

the 1-µm wavelength range (Fig. 1), with pulse durations as short as 100 fs combined with pulse peak powers in the kW-range at gigahertz repetition rates. The performance of modelocked SDLs has become comparable with fiber, Ti:sapphire, and diode-pumped solid state lasers. Many applications have been demonstrated such as multi-photon imaging [15,16] and frequency comb metrology [17–20].

Here, we investigate the complex multipulse instabilities of a high-power 100-fs SESAM-modelocked VECSEL (red circles in Fig. 1) [14]. We carefully analyze different modelocking states and their hysteresis depending on the pump power. We find that the maximum power in fundamental modelocking operation is not limited by thermal effects, but by the onset of multipulse instabilities, where more than one pulse oscillates in the laser cavity. While some applications may tolerate multipulse operation or some minor intensity fluctuations, other applications such as frequency metrology become only possible with low intensity noise, low timing jitter, or even a stabilized carrier envelope offset frequency [21]. Stable modelocking with excellent low noise operation has been demonstrated for such lasers [22,23]. The onset of multipulse operation currently limits the output power and a better understanding is required to further scale the power in fundamental modelocking. Additionally, the multipulse analysis provides new insights in the physics of highly inverted semiconductor structures at the timescale of 100 fs, where interesting effects start to play a role, such as kinetic hole burning, theoretically predicted by fully microscopic many-body models [24,25]. Comprehensive modelocking characterization allows us to compare the different modelocking states. The similarity of single measurement parameters for different modelocking states shows the importance of a clean and complete characterization to proof fundamental modelocking, as described in [26,27]. Finally, with an extensive characterization of the nonlinear reflectivity of the VECSEL and SESAM, we can show that the onset of multipulse operation occurs at the roll-over of the total cavity round trip reflectivity.

2. Characterization

The VECSEL used for the more detailed investigation of multipulse dynamics can generate stable 100-fs pulses in fundamental modelocking and has been described in [14]. We operate the laser in the same configuration that allowed the shortest pulses reported in [14] (i.e. same SESAM and VECSEL chips, same cavity design and heat-sink temperatures), however, we then continued to increase the pump power.

We observe that, once the laser has reached a certain maximum average output power in fundamental modelocking operation, more pump power does not simply increase of average output power with the same slope efficiency. Before thermal roll-over starts to occur, we observe several steps in increased output power with different modelocking states for which multiple pulses simultaneously oscillate in the cavity. We also observe a hysteresis effect for which these modelocking states depend on the pump history with continuously increased or decreased pump power (Fig. 2). To carefully analyze every modelocking state, we therefore characterized the laser performance at different pump powers. Clear discontinuities in average output power appear when ramping up the pump power [Fig. 2(a)], which also indicate a new modelocking regime [Fig. 2(b)].

Increasing the pump intensity starting from a low level, we observe a first threshold at a pump power of 20 W, where lasing action in fundamental modelocking begins. Then at 22.6 W, we observe an abrupt increase of the average output power by a factor of 1.6 and, similarly, new discontinuities are observed at 24.8 W and 27 W. A clear hysteresis effect is observed when starting from a high pump level and continuously decreasing the pump power during which we do not reproduce the same average output power and also not in all cases the same multipulse state. Compared to the “increasing pump path”, the laser delivers a higher average output power when the pump is between 27.7 and 22.9 W. Fundamental modelocking

Optics EXPRESS

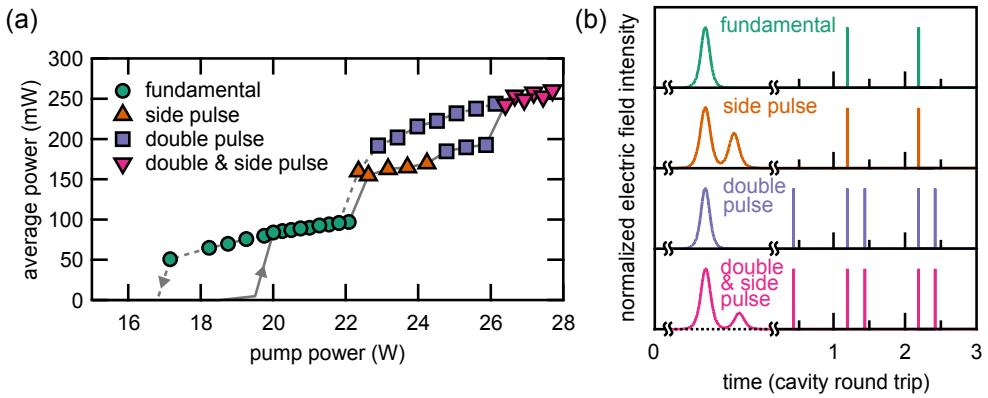

Fig. 2. (a) Average output power from a SESAM modelocked VECSEL measured for increasing (solid line) and decreasing (dashed line) pump power. (Markers) measurement points color coded according to their modelocking state: (green circle) *fundamental*, (orange triangle) *side pulse*, (violet square) *double pulse*, and (pink triangle) *double & side pulse* operation. (b) Representative electric field intensity for the corresponding modelocking states with a zoom into the first pulse: (green) *fundamental*, (orange) *side pulse*, (violet) *double pulse*, and (pink) *double & side pulse*. The side pulse visible in the zoom is below the resolution on the cavity round trip scale.

operation, with only one pulse per cavity round trip, extends to a lower pump power of 17.2 W. Hysteresis behaviors for SDLs in modelocking operation were already reported for picosecond pulses [28]. However, the femtosecond modelocking states we want to analyzed here [Fig. 2(b)] differ from what was previously characterized and are referred to as:

- *Fundamental modelocking:* One single pulse oscillates in the laser cavity.
- *Side pulse:* An additional side pulse close to the main pulse with a temporal spacing much shorter than the cavity round trip time.
- *Double pulse:* Two pulses oscillate in the laser cavity, spaced by approximately a quarter of the cavity round trip time.
- *Double & side pulse:* A combination of *side pulse* and *double pulse* operation, where we have two pulse groups or a pulse and a pulse group separated by approximately a quarter of the cavity round trip time similar to the *double pulse* operation. The pulse groups features a main pulse accompanied by a side pulse similar to the *side pulse* operation. The total number of pulses adds up to three or four pulses.

2.1 Pulse duration

The pulse duration is measured with a non-collinear second-harmonic generation (SHG) autocorrelation (FR-103MN from *Femtochrome Research, Inc)*. The autocorrelation traces of the *fundamental* and the *double pulse* states [Fig. 3(a)] are fitted with the autocorrelation of a sech^2-pulse with a pulse duration τ_{pulse}. They feature one single pulse, whereas the autocorrelation of the *side pulse* and *double & side pulse* states indicates the presence of two pulses next to each other [Fig. 3(a)]. These traces can be fitted with two subsequent sech^2-pulses separated by τ_{sep} with an asymmetric intensity ratio of the two pulses [Fig. 3(b)].

The pulse duration of the *fundamental* state reaches the minimum value just before the transition to *side pulse* operation [Fig. 4(a)], as the laser cavity is optimized for the shortest pulse duration in fundamental modelocking at the highest possible average power. The pulse durations of the *side pulse* and *double & side pulse* states are slightly longer with a side pulse

Optics EXPRESS

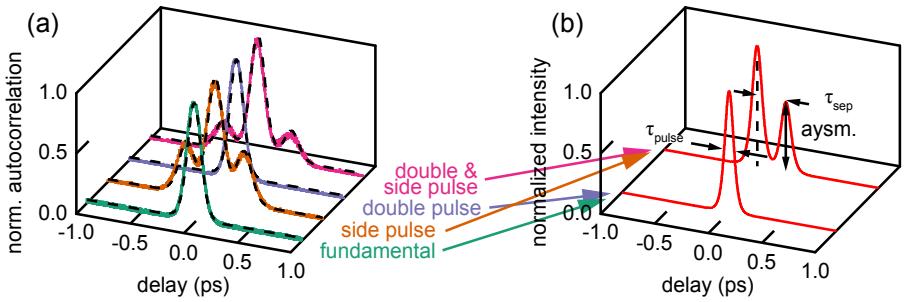

Fig. 3. (a) Normalized autocorrelation measurement for each of the four modelocking states (colored solid line) with the corresponding fit (black dashed line). (b) Pulse fit function in the time domain featuring one sech^2-pulse or two consecutive sech^2-pulses with a pulse separation τ_{sep} and an asymmetric intensity ratio.

asymmetry of roughly 61% and 27%, respectively. We also remark that the separation of the side pulse increases with increasing pump power from 270 to 340 fs. For the *double pulse* state, the pulse duration is shorter again, similar to the values observed for the *fundamental* state [Fig. 4(a)]. Interestingly, sweeping the hysteresis path going down from high pump intensity, we obtain even shorter pulse durations (94 fs instead of 96 fs) for the *fundamental* state when we reach it from a multipulse state [Fig. 4(a)].

2.2 Optical spectrum

The optical spectrum is measured with a fiber coupled optical spectrum analyzer HP 70952B with a resolution of 0.1 nm [Fig. 5(a)]. All optical spectra show no indication of any instability or continuous wave breakthroughs. While the optical spectra are almost sech^2-shaped for the *fundamental* and *double pulse* states, the optical spectra of the *side pulse* and *double & side pulse* states feature shoulders on both the short and long wavelength side. The center wavelength shifts almost linearly (0.65 nm/W) to higher wavelengths with increasing

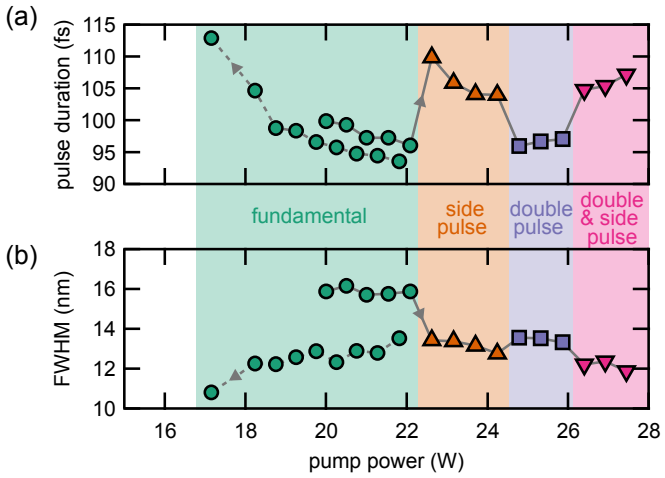

Fig. 4. (a) Pulse duration measured for increasing (solid line) and decreasing (dashed line) pump powers. (b) Corresponding full width at half maximum (FWHM) of the optical spectrum for (solid line) increasing and (dashed line) decreasing pump powers.

Optics EXPRESS

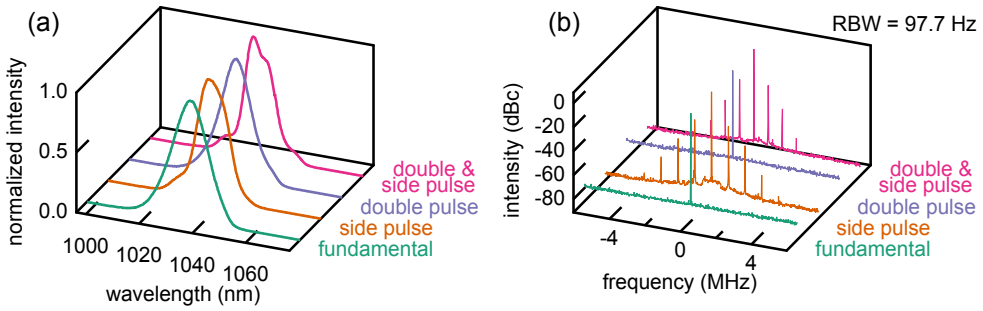

Fig. 5. (a) Optical spectra of the different modelocking states measured with a 0.1 nm resolution. (b) Microwave spectrum of the laser intensity showing first harmonic of the repetition rate for the different modelocking states measured with a resolution bandwidth (RBW) of 97.7 Hz.

pump power. The *fundamental* state features the broadest spectral full width at half maximum (FWHM), while the multipulse states at higher pump powers have a narrower spectrum [Fig. 4(b)]. Interestingly, the optical bandwidths of the *fundamental* states are reduced (from 15.9 nm to 13.5 nm) after the back transition from multipulse states. Combined with the shorter pulse duration, this corresponds to a decrease of the time-bandwidth product from 0.43 to 0.34 at the center wavelength of 1035 nm. Which means that the chirp of the pulse substantially changed while the average output power of 96 mW stayed the same.

2.3 Noise characterization

The first harmonic of the pulse repetition rate is analyzed with the signal source analyzer E5052B from *Agilent* with a resolution bandwidth of 97.7 Hz resulting in a high signal-to-noise ratio of approximately 80 dB. For this, the laser intensity is measured with a highly linear photodiode (HLPD from *Discovery Semiconductor*). The microwave spectra are centered around the pulse repetition rate of 1.641 GHz with a span of 10 MHz [Fig. 5(b)]. For the *fundamental* and the *double pulse* states, the microwave spectra feature a delta like peak, without any visible broadening or pedestal, as it is theoretically expected for stable fundamental modelocking. The *side pulse* and *double & side pulse* states can be clearly identified by the 3 pairs of side peaks below −25 dBc next to the main peak of the pulse repetition rate. The side peak separation is 0.95 and 0.81 MHz for the *double pulse* and *double & side pulse* state, respectively. These side peaks indicate a modulation of the pulse train intensity. We assume an intensity variation of the main and the side pulse similar to the

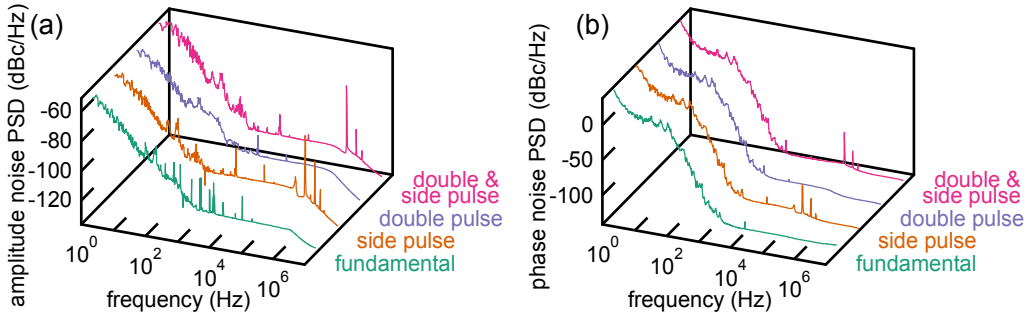

Fig. 6. (a) Amplitude noise and (b) phase noise power spectral density (PSD) of the first harmonic of the repetition rate for the different modelocking states.

Optics EXPRESS

irregular pulse train with varying intensities predicted by the simulation result descried in section 3.1 and illustrated in Fig. 8(b). The intensity modulation of the pulse train is further revealed by the additional noise peaks in the amplitude and phase noise at the given frequencies (Fig. 6). The amplitude and phase noise of the first harmonic of the repetition rate is measured using the same signal source analyzer.

2.4 Temporal dynamics

So far, the presented measurements do not differentiate between the *fundamental* and the *double pulse* state or between the *side pulse* and the *double & side pulse* state. But, a difference becomes evident when looking at the laser intensity over several cavity round trip times [Fig. 7(a)]. The time traces are measured with a sequential equivalent-time sampling scope (CSA 803 from *Tektronix* with a 50-GHz sampling unit SD-32) and a high-speed photodetector (Model 1454 from *Newport* with an 18.5-ps rise time) amplified by an 18-GHz bandwidth preamplifier (87405C from *Agilent*).

While for *fundamental* and the *side pulse* state one pulse per round trip is measured, an additional pulse is observed for the *double pulse* and the *double & side pulse* state. In contrast to second harmonic modelocking where the separation of the additional pulse is given by one half of the round trip time [28], the additional pulse is separated by one quarter of the round trip time. For the *side pulse* and *double & side pulse* states, the pulse separation τ_{sep} is too small and cannot be resolved with the sampling scope. Only when we characterize the modelocking with both the autocorrelation and the sampling scope we can directly observe the full number of pulses simultaneously oscillating in the cavity (i.e. one pulse for the *fundamental*, two for the *side pulse*, two for the *double pulse*, and four for the *double & side pulse* state).

The dynamics of the VECSEL is further characterized by a microwave spectrum analyzer (8565EC from *Agilent*) using the same high-speed photodetector and preamplifier. A stable fundamentally modelocked laser creates equally powerful harmonic peaks positioned at the repetition rate and at multiples of the repetition rate as measured for the *fundamental* and *side pulse* states [Fig. 7(b)], only limited by the bandwidth of the preamplifier for frequencies >18 GHz. Again, the two pulses separated by τ_{sep} of the *side pulse* and *double & side pulse* state are below the resolution of the photodetector and therefore are not resolved in the microwave spectrum measurement. For the *double pulse* and *double & side pulse* states, where the pulses are spaced by a quarter of the round trip time, the higher harmonics are periodically modulated [Fig. 7(b)]. This stands in contrast to second harmonic modelocking, where only even harmonics would be visible and the fundamental frequency, corresponding to the inverse of the cavity round trip time, would not be visible at all.

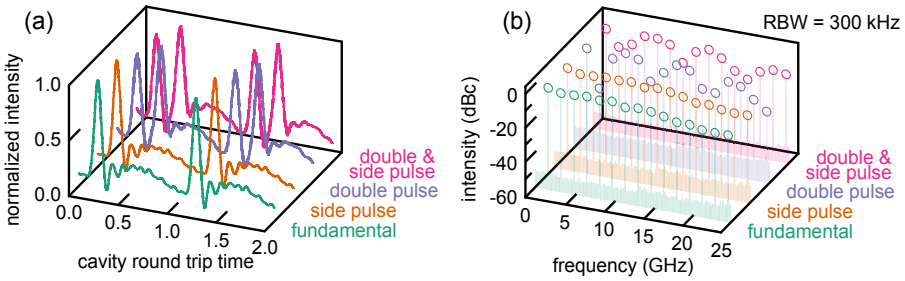

Fig. 7. (a) Laser intensity time traces of the different modelocking states measured with a sampling scope. For the *double pulse* and the *double & side pulse* state an additional peak is visible, separated by roughly one quarter of the cavity round trip time. (b) Microwave spectrum of the laser intensity showing the high harmonics of the repetition rate for the different modelocking states measured with a resolution bandwidth (RBW) of 300 kHz. For better visibility, the peak maxima are highlighted with circles.

Optics EXPRESS

3. Discussion

3.1 Hysteresis

The modelocking analysis reveals different hysteresis effects. Similar to what was reported for the antiresonant gain medium design in [28], we see a large hysteresis loop of the *fundamental* state, such that the stable fundamental modelocking continues far below the original threshold [Fig. 2(a)]. Smaller hysteresis loops are observed for the other modelocking states. The *double pulse* state is special. It is more stable than the *side pulse* state and sometimes it switches directly back to fundamental modelocking, if the pump power is reduced. The *double pulse* states also have an increased average power with slightly longer pulses during the "decreasing pump path" when compared to the "increasing pump path".

Interesting is also the hysteresis of the *fundamental* states which have shorter pulse durations with narrower spectral bandwidths on the "decreasing pump path". This shows that different stable modelocking states can exist for one given pump power. These features are going beyond the theoretical predictions of a fully microscopic many-body simulation [25].

To gain insights into the dynamical formation and stability of different modelocked pulse trains, we are using a simulation based on coupled multi-delay differential equations. In contrast to the delay model widely used for a ring cavity modelocked laser [29–31], our modeling approach considers the geometry of the V-shape without the need to change to the numerically demanding traveling wave approach. Previous works on VECSEL simulations either do not consider the effects induced by the cavity geometry [32,33] or do not allow for an efficient simulation of large external cavities [25,34]. To obtain our numerically efficient description of the VECSEL dynamics, we integrate the traveling-wave equation for the electric field amplitude $E^{\pm}(z, t)$ and the excess charge-carrier density $N(z, t)$ [35]

$$\left(\partial_t \pm \frac{1}{v_g}\partial_z\right) E^{\pm}(z,t) = \left[-\frac{\alpha_{\text{int}}}{2} + \frac{1}{2}N(z,t)\right] \cdot E^{\pm}(z,t) \tag{1}$$

along its characteristic curve [36] for small sections Δz. We then consider the limit of infinitely thin gain and SESAM sections with integrated carrier densities $G(t)$ and $Q(t)$. The free space between the optical elements is treated as large passive sections. Expressing the electric fields in all sections in terms of the electric field $A(t)$ at the out-coupling mirror (OC) leads to a system of three coupled multi-delay differential equations Eq. (2)-(4).

$$\frac{d}{dt}A(t) = \gamma \cdot \left(\sqrt{\kappa} \cdot A(t-T) \cdot e^{\frac{1}{2}(G(t-\tau_1)+G(t-\tau_1-2\tau_2))+Q(t-\tau_1-\tau_2)} - A(t)\right) \tag{2}$$

$$\frac{d}{dt}G(t) = J_G - \gamma_G \cdot G(t) - \left(e^{G(t)} - 1\right) \cdot \left(\left|A(t-\tau_1)\right|^2 + \left|A(t-\tau_1-2\tau_2)\right|^2 \cdot e^{2Q(t-\tau_1)+G(t-2\tau_2)}\right) \tag{3}$$

$$\frac{d}{dt}Q(t) = J_Q - \gamma_Q \cdot Q(t) - r_s \cdot (e^{2\cdot Q(t)} - 1) \cdot e^{G(t-\tau_2)} \cdot \left|A(t-\tau_1-\tau_2)\right|^2 \tag{4}$$

Note that these equations, although similar to those presented in [29], contain both propagation directions and the spatial configuration of the VECSEL cavity, which is encoded in the time delays τ_1 and τ_2. Charge-carrier induced amplitude-phase coupling is omitted in this model, but could easily be included for future studies by introducing an alpha-factor in Eq. (1). The gain bandwidth is denoted by γ, the intensity losses per round trip by κ, the cold-cavity round trip time by T, the pump current by J_G, the unsaturated absorption by J_Q, the gain and absorber recovery times by γ_G and γ_Q, and the ratio between the gain and absorber

Optics EXPRESS

Table 1. Parameter values normalized to the round trip time T = 625 ps used to produce the following simulation results

parameter	γ	κ	γ_G	γ_Q	J_Q	r_s
norm. value	2000	0.99	0.625	122.5	–100	2.0

differential by r_s. The delay times are determined by the resonator configuration $\tau_1 = L_{\text{OC-VECSEL}}/v_g$ and $\tau_2 = L_{\text{VECSEL-SESAM}}/v_g$, where $L_{\text{OC-VECSEL}}$ is the distance between OC and VECSEL chip, $L_{\text{VECSEL-SESAM}}$ is the distance between VECSEL chip and SESAM, and v_g is the group velocity. In this model, we use an "ideal" pump current directly setting the electron density for the VECSEL gain, which is simpler than using an optical pump power.

For the parameter values given in Table 1, the laser described with Eq. (2)-(4) exhibits a range of pump currents J_G with stable modelocked pulses whose width directly depend on the gain bandwidth γ and therefore on the number of longitudinal modes that participate in the modelocking process. We choose $\gamma = 2000$, which yields pulses that have a width of about 1-2 ps. This is longer than observed in the experiments, but in order to reach the experimental value much larger γ would be necessary leading to much longer computation times. We use the above value in the following numeric characterization to be able to effectively scan a wide parameter region. Investigations of the effects of larger γ are still ongoing.

This simulation reveals multistability and their hysteresis in a parameter scan of the pump current J_G [Fig. 8(a)]. The dynamics for increasing and decreasing pump current are simulated. For illustration, the pulse peak intensities of a simulated pulse train are shown. We can clearly distinguish three regimes: *fundamental modelocking*, irregular pulse trains, and *double pulse* emission.

The region of irregular pulse trains is characterized by a periodic emission of irregular pulse "cluster" with varying pulse intensities [Fig. 8(b)]. Interestingly, the autocorrelation function determined from these irregular pulsating time series shows similarities with the

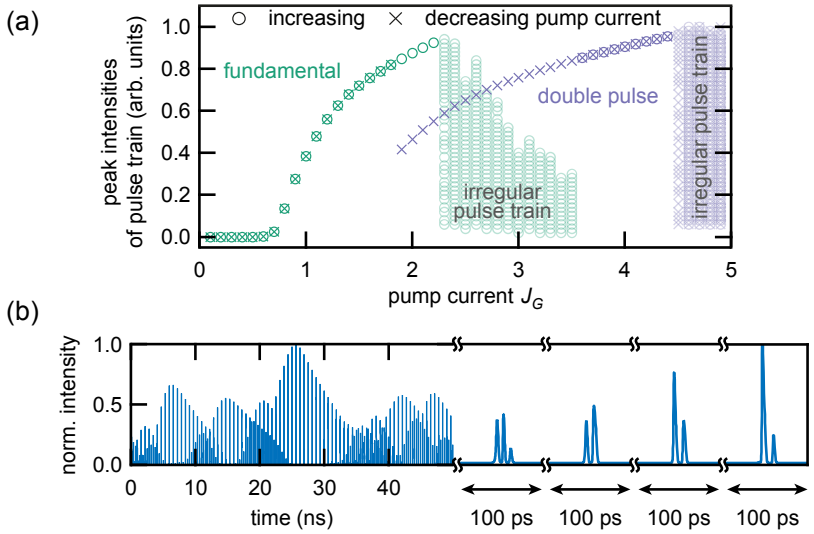

Fig. 8. Simulation results based on the coupled multi-delay differential equations (Eq. (1-4) and Table 1): (a) Peak pulse intensity as a function of pump current. The dynamics for increasing (circle) and decreasing (cross) pump current clearly show *fundamental modelocking* (green), irregular pulse train (light green), and *double pulse* operation (violet). (b) Irregular pulse train as a function of time, on a time scale much larger (left) and much shorter (right) than one cavity round trip.

Optics EXPRESS

experimentally found *side pulse* state, because also in the simulations side pulses show up next to the main peak of the autocorrelation. Due to the chosen gain bandwidth γ, the pulse width is on the picosecond scale and thus also the distance between side and main peak is larger than experimentally observed. However, the similarities to both the experimentally observed parameter region and the measured autocorrelation suggest that these kind of dynamic instabilities can be one reason for the emergence of side pulses in the autocorrelation. An additional explanation of the dynamics behind the observed side pulse regime will be discussed in section. 3.4.

After the region of irregular pulse trains, the laser switches to the double pulse state. Compared to the fundamental state, the intensity of the double pulse states are drastically decreased because for this regime two pulses need to be amplified per round trip. And additionally, the absorber can completely recover between two pulses thus cause increased absorption which leads to a reduced output power. Such that for a given pump current, two double pulses, bistable to a single pulse, carry less combined power than the single pulse. For reducing pump current, the double pulse emission extends in the region of irregular pulse trains, similar to our experiments [Fig. 2(a)].

3.2 Double pulse operation

The two pulses of the *double pulse* state are spaced by roughly one quarter of the cavity round trip time, which differs from second harmonic modelocking where the pulse separation would be half of the cavity round trip time. This *double pulse* operation is similar to the multipulse operation reported in [10]. In both cases a similar modulation of the higher harmonics of the repetition rate is measured with a microwave spectrum analyzer [Fig. 7(b)].

Simulations using the above mentioned coupled multi-delay differential equations indicate that the type of multipulse state strongly depend on the arrangement of the V-shaped laser cavity. Changing the delay times τ_1 and τ_2 corresponds to changing the resonator configuration, i.e. the two arms $L_{\text{OC-VECSEL}}$ and $L_{\text{VECSEL-SESAM}}$ of the V-shaped geometry. By keeping the total cavity length L_{CAVITY} constant, we can scan the gain chip position within the cavity. Varying both the gain chip position and the pump current reveals different stability regions: no lasing, *fundamental* operation, *double pulse* state, second harmonic modelocking, irregular pulse trains, and higher order states. Parameter ranges clearly favoring second harmonic modelocking or the *double pulse* state are found [Fig. 9(a)]. At sufficient pump currents, the laser is expected to operate in the *double pulse* state when the gain chip is placed in the center of the cavity. Whereas, second harmonic modelocking is favored when the gain chip is placed closer to the OC or closer to the SESAM.

This can be explained by looking at the time evolution of the electric field intensity and the evolution of the gain for two cavity geometries [Fig. 9(b)]. The preferred pulse configuration is obtained for the case where the two pulses hit the gain chip are equally spaced in time. This allows for a balanced recovery of the gain between the pulses. Since the recovery of the SESAM absorption is much faster, it is not limiting here. When the gain chip is in the center of the cavity ($L_{\text{OC-VECSEL}}/L_{\text{CAVITY}} = 0.5$) the *double pulse* state is preferred and when the gain chip is closer to the OC or to the SESAM ($L_{\text{OC-VECSEL}}/L_{\text{CAVITY}} = 0.25$ or 0.75) second harmonic modelocking is preferred. For the distance ratio of 0.53 used in the experimental cavity, the favored configuration is the observed *double pulse* state.

Moreover, a central positioning of the gain chip also increases the region of stable fundamental modelocking towards higher pump currents and thereby allows for higher output powers. Similar to the multi-pulse operation, the central configuration ensures equal times between pulse incidents in the gain chip and thus ensures a balanced recovery.

3.3 Cavity round trip reflectivity

To gain a deeper insight of the modelocking mechanisms and the multipulse operation, we investigated in more details the saturation characterization of the VECSEL cavity. Similarly,

Optics EXPRESS

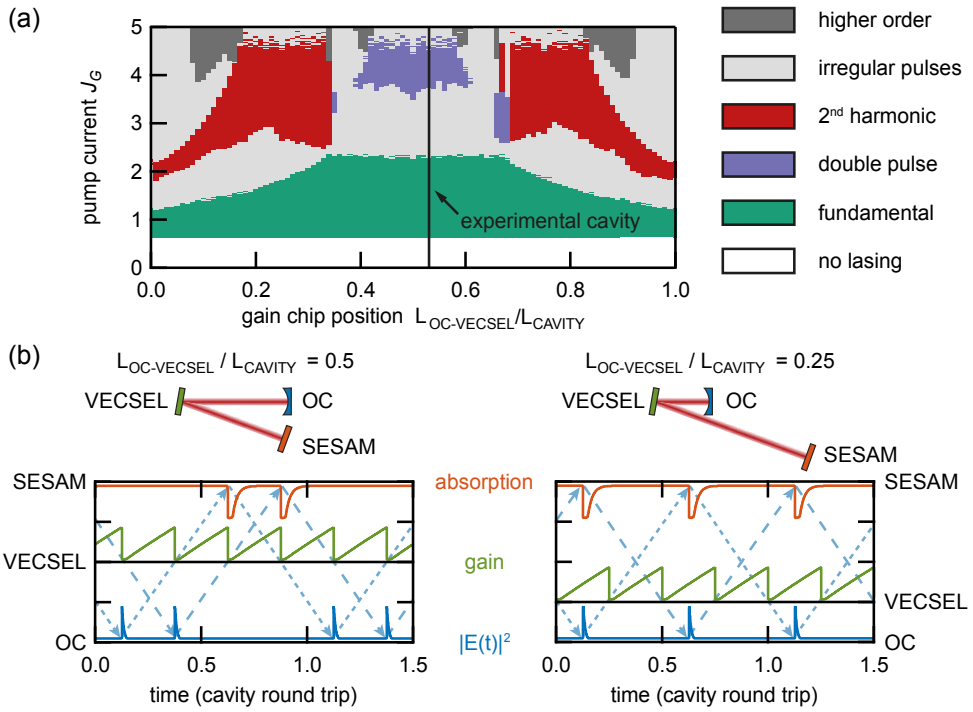

Fig. 9. Simulation results based on the coupled multi-delay differential equations (Eq. (1-4) and Table 1): (a) Simulation for different pump currents and different positions of the gain chip (described by the distant $L_{OC\text{-}VECSEL}$ between the output coupler (OC) and the VECSEL chip at constant total cavity length L_{CAVITY}). The different stability regions are color coded: no lasing (white), *fundamental* state (green), *double pulse* state (violet), second harmonic modelocking (magenta), irregular pulse trains (grey), higher order states (dark grey). The black line indicates the gain chip position in the investigated experimental cavity. (b) Time evolution of the electric field intensity at the OC position (blue), of the VECSEL gain (green), and of the SESAM absorption (orange) shown for the two cavity configurations $L_{OC\text{-}VECSEL}/L_{CAVITY}$ = 0.5 and 0.25.

as described by Alfieri *et al.* [37], we calculate the saturation of the cavity round trip reflectivity by combining the saturation of the VECSEL and the SESAM. For different average output power, we calculate the corresponding intracavity pulse energy given the pulse repetition rate and the output coupler reflectivity. With the know cavity spot size on the VECSEL and the SESAM, we than calculate the corresponding fluences which relate to different reflectivities of the elements. For the cavity round trip reflectivity of the V-shaped cavity, we multiply the output coupler reflectivity with the SESAM reflectivity and with twice the VECSEL reflectivity. The reflectivity saturation of the VECSEL and the SESAM are measured beforehand with 170-fs probe pulses as described in [14]. The VECSEL and the SESAM are characterized for different probing wavelengths, heat-sink temperatures, and optical pump powers. This allows us to estimate the laser saturation for different fundamental modelocking states by interpolation.

We estimated the saturation round trip reflectivity of the *fundamental* state at 20.0 W pump power [Fig. 2(a)] given the measured center wavelength [Fig. 4(b)] and the used heat-sink temperatures of the SESAM and the VECSEL. Compared to the 170-fs probe pulse of the reflectivity measurements, the pulse duration of the *fundamental* state is slightly shorter around 100 fs. It is assumed that the reflectivity is not significantly changed. The measured

Optics EXPRESS

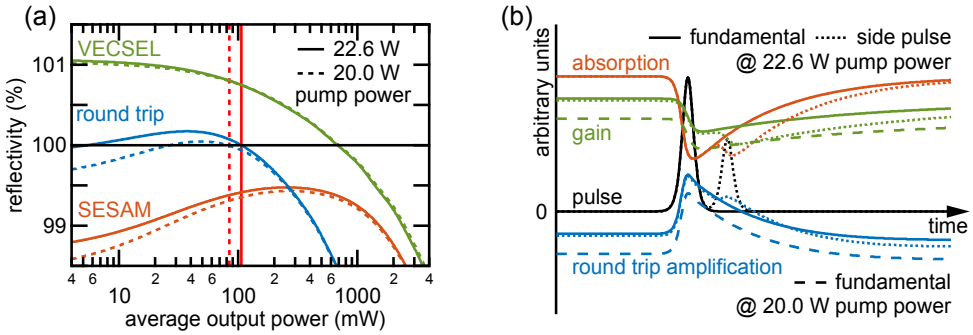

Fig. 10. (a) Estimated reflectivity saturation of the VECSEL chip (green), the SESAM (orange), and the cavity round trip (blue) for fundamental modelocking operation with different average output powers. The saturation is estimated for *fundamental* states in Fig. 2(a). The reflectivity curves are shown for the *fundamental* state at 20.0 W pump power (dashed lines) and for a theoretical *fundamental* state at 22.6 W (solid lines), where in the experiment the laser switched to *side pulse* operation. The stable operation point where the round trip reflectivity is 100% is in good agreement with the corresponding measured average output power (red lines). (b) Simulation (see section 3.4 for more details) of the instantaneous gain of a double passage on the VECSEL chip (green), the instantaneous absorption of the SESAM (orange), and the instantaneous cavity round trip amplification (blue). The simulation shows the response to a 100-fs probe pulse at 20.0 W of pump power (dashed lines) and at 22.6 W pump power (solid lines). In analogy to the *side pulse* state, the response is shown for a 100-fs probe pulse with an additional side pulse separated by 300 fs at 22.6 W pump power (dotted lines).

average output power of 84 mW is in good agreement with the laser saturation estimation. This output power corresponds to an estimated reflectivity of 100% with relates to the stable lasing condition: gain equal loss. The measured output power and the estimated laser operation points are in good agreement for all the *fundamental* states in Fig. 2(a). The estimated laser operation points lie slightly in the roll-over of the round trip reflectivity. This behavior is common for SESAM-modelocked lasers and has been reported for SDLs based on active QWs [37], QDs [38] and for thin disk lasers [39]. It can be seen, that the SESAM is not fully saturated and thus is not operated at the point of minimal loss. Hence, higher output power could be achieved with a fully saturated SESAM. Further investigations are ongoing which address the question: Does a fully saturated SESAM maintain the short pulse duration? However this is beyond the scope of this paper.

To investigate the transition to the *side pulse* state, we calculate the round trip reflectivity at 22.6 W pump power as if the laser would remain in the *fundamental* state [Fig. 10(a)], even though in the experiment the laser would have switched to the *side pulse* state. Despite the increased pump power, the reflectivity, and therefore the gain, of the VECSEL gain chip seems nearly unchanged. The reason is that the additional gain due to higher pumping is balanced by a reduction of gain caused by a red-shift of the laser spectrum with consequently lower gain at longer wavelengths. The red-shift of the laser is also the cause for the reflectivity increase of the SESAM. With this, the theoretical operation point is even further in the roll-over. On the other hand, the reflectivity for low power pulses is increased to nearly 100%. Thus, low power optical noise is not efficiently suppressed anymore. This can destabilize the laser operation, which explains a transition in lasing operation, such as the experimentally observed switch to *side pulse* operation.

This model cannot be extended to the *side pulse* and *double pulse* states as the successive pulses would see a partially saturated VECSEL gain and SESAM absorption and therefore substantially changing the reflectivity.

Optics EXPRESS

3.4 Side pulse operation

On the 100-fs timescale new effects of the semiconductor material start to play a role, such as kinetic hole burning, theoretically predicted by fully microscopic many-body models [24,25]. The related kinetic hole filling can explain the two time scales in the recovery of the VECSEL reflectivity measured in situ during modelocking operation [40]. This in situ measurements revealed an initial fast gain recovery of up to 80% taking place in few hundreds of femtoseconds, followed by a slow recovery in the hundreds of picoseconds determined by the slow refilling of the quantum well by diffusion of the optically pumped carriers.

These 100-fs timescale effects are not included in the coupled multi-delay differential equations introduced in section 3.4. Thus, we implemented another simpler rate equation model to study the fast quantum well dynamics, as described in [37]. This model cannot describe modelocking formation, but it describes the instantaneous response to an incoming pulse for both the gain of the VECSEL chip and the absorption of the SESAM. This allows for an estimation of the instantaneous round trip amplification, by considering two passes on the VECSEL chip, one pass on the SESAM, and taking into account all the cavity losses, such as the output coupler loss.

This simulation shows that for a 100-fs pulse at 20.0 W pump power the round trip amplification is limited to the temporal pulse width [Fig. 10(b)]. But for 22.6 W pump power, the instantaneous round trip amplification stays positive for an interval after the trailing edge of the pulse. Thus, the combination of the initial fast recovery of the gain and the partially saturated SESAM from the first pulse supports a weaker side pulse to reach lasing threshold. The corresponding simulation for a 100-fs probe pulse with an additional delayed side pulse separated by 300 fs reveals the increased positive instantaneous amplification for the side pulse, which enables the experimentally observed *side pulse* operation.

Side pulse operations have also been reported for example in a colliding pulse cavity or with a graphene saturable absorber [41,42]. The optical spectra of these previously reported results look like the combination of two spectra with different center wavelength. However in our case, the optical spectra of the *side pulse* states are still close to sech^2-shaped with only two small shoulders on the side [Fig. 5(a)].

4. Conclusion

In conclusion, we present an analysis of the pump power dependent modelocking performance of a SESAM-modelocked VECSEL. We identify four different modelocking states correlated with a step-like increase of the average output power. Besides an initial *fundamental modelocking* state, we find stable multipulse operations, such as *side pulse*, *double pulse*, and *double & side pulse* states. A single characterization technique is not sufficient to distinguish between all these different modelocking states. Therefore, we can confirm again that modelocking results obtained with SDLs must be accompanied by a comprehensive characterization, similar to the findings in [26,27]. *Side pulse* operation can be distinguished from fundamental modelocking by side peaks in the autocorrelation, by shoulders in the optical spectrum, by side peaks next to the repetition rate in the microwave measurement, and by additional peaks in the amplitude and phase noise. On the other hand, the *double pulse* state can only be distinguished from fundamental modelocking by a time trace measured with a fast photodiode and by an oscillating signal strength of the harmonics of the repetition rate. The change in signal strength of the harmonics is less pronounced as for second harmonic modelocking where all odd harmonics are missing.

The modelocking analysis reveals interesting hysteresis effects, such as a hysteresis loops of the different modelocking states and also a shortening of the pulse duration combined with a narrower optical spectrum of the *fundamental* state when operating in the “decreasing pump path” of the hysteresis curve [Fig. 2(a)].

At higher pump power beyond stable fundamental modelocking, simulations show that the type of multipulse state strongly depends on the cavity arrangement. Different multipulse

Optics EXPRESS

operation can be obtained with different gain chip positions within the cavity round trip. Operation is optimized when the two pulses hit the gain chip equally spaced in time. The highest power in fundamental modelocking is therefore achieved when the VECSEL gain chip is centered in the cavity (Fig. 9).

To improve the average output power of fundamental modelocking, which in our case is not limited by thermal effects but by multipulse instabilities, we have investigated the onset of multipulse instabilities in great detail. We find that the transition to multipulse states takes place in the roll-over of the cavity round trip reflectivity resulting from the interplay between the saturation of the VECSEL gain and the saturation of the SESAM absorption. The combination of the rapid filling of the kinetic hole in the electron-hole distribution, burned by the short femtosecond pulses, and the partially saturated SESAM by the first pulse favors the onset of a weaker side pulse. To prevent these *side pulse* operations, one could use a SESAM with a faster recovery time. Another possibility could be to operate the laser in a chirped pulse configuration with a slow SESAM, which would reduce the effect of kinetic hole burning and simultaneously increase the efficiency of the laser. Further increase in power could also be achieved by increasing the round trip reflectivity which would sustain a higher output coupler transmission. The cavity round trip reflectivity is mainly limited by the saturation of the VECSEL gain.

Funding

Swiss Confederation Program (Nano-Tera.ch); German Research Foundation (DFG) (Collaborative Research Centre 787).

Acknowledgments

We thank the technology and cleanroom facility FIRST of ETH Zürich for advanced micro- and nanotechnology. This work was financed by the Swiss Confederation Program Nano-Tera.ch, which was scientifically evaluated by the Swiss National Science Foundation (SNSF) and by the German Research Foundation (DFG) within the framework of Collaborative Research Centre 787.

References

1. M. Guina, A. Rantamäki, and A. Härkönen, "Optically pumped VECSELs: review of technology and progress," J. Phys. D Appl. Phys. **50**(38), 383001 (2017).
2. M. Kuznetsov, F. Hakimi, R. Sprague, and A. Mooradian, "High-Power (>0.5-W CW) Diode-Pumped Vertical-External-Cavity Surface-Emitting Semiconductor Lasers with Circular TEM00 Beams," IEEE Photonics Technol. Lett. **9**(8), 1063–1065 (1997).
3. B. Rudin, A. Rutz, M. Hoffmann, D. J. H. C. Maas, A.-R. Bellancourt, E. Gini, T. Südmeyer, and U. Keller, "Highly efficient optically pumped vertical-emitting semiconductor laser with more than 20 W average output power in a fundamental transverse mode," Opt. Lett. **33**(22), 2719–2721 (2008).
4. B. Heinen, T. L. Wang, M. Sparenberg, A. Weber, B. Kunert, J. Hader, S. W. Koch, J. V. Moloney, M. Koch, and W. Stolz, "106 W continuous-wave output power from vertical-external-cavity surface-emitting laser," Electron. Lett. **48**(9), 516 (2012).
5. U. Keller, K. J. Weingarten, F. X. Kärtner, D. Kopf, B. Braun, I. D. Jung, R. Fluck, C. Hönninger, N. Matuschek, and J. Aus der Au, "Semiconductor saturable absorber mirrors (SESAMs) for femtosecond to nanosecond pulse generation in solid-state lasers," IEEE J. Sel. Top. Quantum Electron. **2**(3), 435–453 (1996).
6. S. Hoogland, S. Dhanjal, A. C. Tropper, J. S. Roberts, R. Häring, R. Paschotta, F. Morier-Genoud, and U. Keller, "Passively mode-locked diode-pumped surface-emitting semiconductor laser," IEEE Photonics Technol. Lett. **12**(9), 1135–1137 (2000).
7. B. W. Tilma, M. Mangold, C. A. Zaugg, S. M. Link, D. Waldburger, A. Klenner, A. S. Mayer, E. Gini, M. Golling, and U. Keller, "Recent advances in ultrafast semiconductor disk lasers," Light Sci. Appl. **4**(7), e310 (2015).
8. M. A. Gaafar, A. Rahimi-Iman, K. A. Fedorova, W. Stolz, E. U. Rafailov, and M. Koch, "Mode-locked semiconductor disk lasers," Adv. Opt. Photonics **8**(3), 370–400 (2016).
9. A. Rahimi-Iman, "Recent advances in VECSELs," J. Opt. **18**(9), 093003 (2016).
10. M. Butkus, E. A. Viktorov, T. Erneux, C. J. Hamilton, G. Maker, G. P. A. Malcolm, and E. U. Rafailov, "85.7 MHz repetition rate mode-locked semiconductor disk laser: fundamental and soliton bound states," Opt. Express **21**(21), 25526–25531 (2013).

Optics EXPRESS

11. M. Mangold, C. A. Zaugg, S. M. Link, M. Golling, B. W. Tilma, and U. Keller, "Pulse repetition rate scaling from 5 to 100 GHz with a high-power semiconductor disk laser," Opt. Express **22**(5), 6099–6107 (2014).
12. O. Casel, D. Woll, M. A. Tremont, H. Fuchs, R. Wallenstein, E. Gerster, P. Unger, M. Zorn, and M. Weyers, "Blue 489-nm picosecond pulses generated by intracavity frequency doubling in a passively mode-locked optically pumped semiconductor disk laser," Appl. Phys. B **81**(4), 443–446 (2005).
13. A. Härkönen, C. Grebing, J. Paajaste, R. Koskinen, J. P. Alanko, S. Suomalainen, G. Steinmeyer, and M. Guina, "Modelocked GaSb disk laser producing 384 fs pulses at 2 µm wavelength," Electron. Lett. **47**(7), 454–455 (2011).
14. D. Waldburger, S. M. Link, M. Mangold, C. G. E. Alfieri, E. Gini, M. Golling, B. W. Tilma, and U. Keller, "High-power 100 fs semiconductor disk lasers," Optica **3**(8), 844–852 (2016).
15. R. Aviles-Espinosa, G. Filippidis, C. Hamilton, G. Malcolm, K. J. Weingarten, T. Südmeyer, Y. Barbarin, U. Keller, S. I. C. O. Santos, D. Artigas, and P. Loza-Alvarez, "Compact ultrafast semiconductor disk laser: targeting GFP based nonlinear applications in living organisms," Biomed. Opt. Express **2**(4), 739–747 (2011).
16. F. F. Voigt, F. Emaury, P. Bethge, D. Waldburger, S. M. Link, S. Carta, A. van der Bourg, F. Helmchen, and U. Keller, "Multiphoton in vivo imaging with a femtosecond semiconductor disk laser," Biomed. Opt. Express **8**(7), 3213–3231 (2017).
17. C. A. Zaugg, A. Klenner, M. Mangold, A. S. Mayer, S. M. Link, F. Emaury, M. Golling, E. Gini, C. J. Saraceno, B. W. Tilma, and U. Keller, "Gigahertz self-referenceable frequency comb from a semiconductor disk laser," Opt. Express **22**(13), 16445–16455 (2014).
18. P. Brochard, N. Jornod, S. Schilt, V. J. Wittwer, S. Hakobyan, D. Waldburger, S. M. Link, C. G. E. Alfieri, M. Golling, L. Devenoges, J. Morel, U. Keller, and T. Südmeyer, "First investigation of the noise and modulation properties of the carrier-envelope offset in a modelocked semiconductor laser," Opt. Lett. **41**(14), 3165–3168 (2016).
19. S. M. Link, D. J. H. C. Maas, D. Waldburger, and U. Keller, "Dual-comb spectroscopy of water vapor with a free-running semiconductor disk laser," Science **356**(6343), 1164–1168 (2017).
20. N. Jornod, K. Gürel, V. J. Wittwer, P. Brochard, S. Hakobyan, S. Schilt, D. Waldburger, U. Keller, and T. Südmeyer, "Carrier-envelope offset frequency stabilization of a gigahertz semiconductor disk laser," Optica **4**(12), 1482–1487 (2017).
21. H. R. Telle, G. Steinmeyer, A. E. Dunlop, J. Stenger, D. H. Sutter, and U. Keller, "Carrier-envelope offset phase control: A novel concept for absolute optical frequency measurement and ultrashort pulse generation," Appl. Phys. B **69**(4), 327–332 (1999).
22. V. J. Wittwer, R. van der Linden, B. W. Tilma, B. Resan, K. J. Weingarten, T. Sudmeyer, and U. Keller, "Sub-60-fs Timing Jitter of a SESAM Modelocked VECSEL," IEEE Photonics J. **5**, 1400107 (2013).
23. M. Mangold, S. M. Link, A. Klenner, C. A. Zaugg, M. Golling, B. W. Tilma, and U. Keller, "Amplitude Noise and Timing Jitter Characterization of a High-Power Mode-Locked Integrated External-Cavity Surface Emitting Laser," IEEE Photonics J. **6**, 1–9 (2014).
24. J. Hader, M. Scheller, A. Laurain, I. Kilen, C. Baker, J. V. Moloney, and S. W. Koch, "Ultrafast non-equilibrium carrier dynamics in semiconductor laser mode-locking," Semicond. Sci. Technol. **32**(1), 013002 (2017).
25. I. Kilen, S. W. Koch, J. Hader, and J. V. Moloney, "Non-equilibrium ultrashort pulse generation strategies in VECSELs," Optica **4**(4), 412–417 (2017).
26. M. Mangold, M. Golling, E. Gini, B. W. Tilma, and U. Keller, "Sub-300-femtosecond operation from a MIXSEL," Opt. Express **23**(17), 22043–22059 (2015).
27. K. G. Wilcox and A. C. Tropper, "Comment on SESAM-free mode-locked semiconductor disk laser," Laser Photonics Rev. **7**(3), 422–423 (2013).
28. E. J. Saarinen, J. Lyytikäinen, and O. G. Okhotnikov, "Hysteresis and multiple pulsing in a semiconductor disk laser with a saturable absorber," Phys. Rev. E **78**(1), 016207 (2008).
29. A. G. Vladimirov and D. Turaev, "Model for passive mode locking in semiconductor lasers," Phys. Rev. A **72**(3), 033808 (2005).
30. C. Otto, L. C. Jaurigue, E. Schöll, and K. Lüdge, "Optimization of Timing Jitter Reduction by Optical Feedback for a Passively Mode-Locked Laser," IEEE Photonics J. **6**(5), 1–14 (2014).
31. L. Jaurigue, B. Krauskopf, and K. Lüdge, "Multipulse dynamics of a passively mode-locked semiconductor laser with delayed optical feedback," Chaos **27**(11), 114301 (2017).
32. M. Marconi, J. Javaloyes, S. Balle, and M. Giudici, "Passive Mode-Locking and Tilted Waves in Broad-Area Vertical-Cavity Surface-Emitting Lasers," IEEE J. Sel. Top. Quantum Electron. **21**(1), 85–93 (2015).
33. S. V. Gurevich and J. Javaloyes, "Spatial instabilities of light bullets in passively-mode-locked lasers," Phys. Rev. A **96**(2), 023821 (2017).
34. J. Mulet and S. Balle, "Mode-Locking Dynamics in Electrically Driven Vertical-External-Cavity Surface-Emitting Lasers," IEEE J. Quantum Electron. **41**(9), 1148–1156 (2005).
35. B. Tromborg, H. E. Lassen, and H. Olesen, "Traveling wave analysis of semiconductor lasers: modulation responses, mode stability and quantum mechanical treatment of noise spectra," IEEE J. Quantum Electron. **30**(4), 939–956 (1994).
36. A. G. Vladimirov, A. S. Pimenov, and D. Rachinskii, "Numerical Study of Dynamical Regimes in a Monolithic Passively Mode-Locked Semiconductor Laser," IEEE J. Quantum Electron. **45**(5), 462–468 (2009).
37. C. G. E. Alfieri, D. Waldburger, S. M. Link, E. Gini, M. Golling, G. Eisenstein, and U. Keller, "Optical efficiency and gain dynamics of modelocked semiconductor disk lasers," Opt. Express **25**(6), 6402–6420 (2017).

Optics EXPRESS

38. C. G. E. Alfieri, D. Waldburger, M. Golling, and U. Keller, "High-power Sub-300-Femtosecond Quantum Dot Semiconductor Disk Lasers," IEEE Photonics Technol. Lett. **30**(6), 525–528 (2018).
39. I. J. Graumann, A. Diebold, C. G. E. Alfieri, F. Emaury, B. Deppe, M. Golling, D. Bauer, D. Sutter, C. Kränkel, C. J. Saraceno, C. R. Phillips, and U. Keller, "Peak-power scaling of femtosecond Yb:Lu2O3 thin-disk lasers," Opt. Express **25**(19), 22519–22536 (2017).
40. C. Baker, M. Scheller, S. W. Koch, A. R. Perez, W. Stolz, R. J. Jones, and J. V. Moloney, "*In situ* probing of mode-locked vertical-external-cavity-surface-emitting lasers," Opt. Lett. **40**(23), 5459–5462 (2015).
41. A. Laurain, R. Rockmore, H.-T. Chan, J. Hader, S. W. Koch, A. R. Perez, W. Stolz, and J. V. Moloney, "Pulse interactions in a colliding pulse mode-locked vertical external cavity surface emitting laser," J. Opt. Soc. Am. B **34**(2), 329–337 (2017).
42. S. Husaini and R. G. Bedford, "Graphene saturable absorber for high power semiconductor disk laser mode-locking," Appl. Phys. Lett. **104**(16), 161107 (2014).